npj | climate and atmospheric science

Article

Published in partnership with CECCR at King Abdulaziz University

https://doi.org/10.1038/s41612-024-00818-8

Elucidating key factors in regulating budgets of ozone and its precursors in atmospheric boundary layer

Xin Song[1], Xiao-Bing Li[1] ✉, Bin Yuan[1] ✉, Xianjun He[1], Yubin Chen[1], Sihang Wang[1], Yibo Huangfu[1], Yuwen Peng[1], Chunsheng Zhang[2], Aiming Liu[2], Honglong Yang[2], Chanfang Liu[3], Jin Li[1] & Min Shao[1]

The vertical variations and key drivers of ozone and its precursors, namely NOx and VOCs, in the atmospheric boundary layer, have vital impacts on surface ozone budgets but are poorly understood so far. Using online gradient measurements from a 356 m tower, we obtained continuous vertical profiles of ozone and its precursors, which exhibited strong gradients throughout the day. In the daytime, the vertical gradients of ozone precursors are significantly regulated by reactions with OH radicals. At night, our observations confirmed more intense VOC reactions with NO_3 radicals in the residual layer than in the boundary layer. Additionally, we found that residual layer entrainment could contribute to over half of the boundary-layer ozone enhancements in the morning periods. Our results underscore the importance of considering vertical changes of ozone and its precursors in the atmospheric boundary layer when developing future ozone mitigation strategies.

High concentrations of ozone have become a pervasive environmental issue in many cities worldwide[1–6], posing serious threats to human health and crop yields[7,8]. The Clean Air Action Plan initiated in China in 2013 led to rapid decreases in anthropogenic emissions, resulting in notable reductions in ambient concentrations of nitrogen oxides (NOx) and fine particulate matter ($PM_{2.5}$)[4,9]. However, surface ozone levels have not decreased in many cities[4,10,11] due to the uncoordinated control of NOx and volatile organic compounds (VOCs)[12]. Ozone pollution abatement remains a challenging problem for China and many regions around the world at present[6,13–16].

The basis of ozone pollution alleviation lies in deciphering the fundamental factors that govern the budgets of ozone and its precursors throughout the entire atmospheric boundary layer. The majority of previous studies on ozone and its precursors were primarily conducted based on ground-level measurements, owing to the cost and complexity of monitoring techniques and the scarcity of suitable platforms[17]. Nevertheless, many studies have reported differences in the vertical distributions of ozone and its precursors within the atmospheric boundary layer, which can directly or indirectly influence the emergence of pollution episodes at ground level[18–21]. The mechanisms of ozone formation at different altitudes, along with the vertical transport of ozone and its precursors, remain unclear due to insufficient vertical observations[17,22]. Consequently, a comprehensive understanding of the vertical distributions and influencing factors of ozone and its precursors is pivotal for developing effective ozone control strategies[9,23].

In the majority of prior studies, the vertical variations in concentrations of ozone and its precursors were described qualitatively, without presenting quantitative assessment results[24–26]. The budgets of ozone and its precursors at various altitudes within the atmospheric boundary differ substantially due to variations in their sources and sinks. but they are also closely coupled due to enhanced turbulence vertical mixing. As crucial precursors of ozone, ambient VOCs are contributed by complex sources, including both primary emissions and secondary formation and are composed of myriad species with substantial disparities in chemical reactivities[27–29]. Notable differences exist in the vertical distribution of distinct VOC types[30–33]. The vertical variations in both concentrations and compositions of VOCs could influence the budget and recycling of atmospheric radicals, such as hydroxyl (OH) and peroxy (RO_2) radicals, thereby affecting the formation mechanisms (namely VOCs-limited, NOx-limited, and transitional regimes) and production rates of ozone[34–36]. Therefore, clarifying the vertical variations and key drivers of different VOC species is vital for a deep understanding of ozone formation within the atmospheric boundary layer.

The vertical variations in concentrations of many VOC species have been reported using gradient observations from various measurement techniques such as tethered balloons, towers, aircraft, and unmanned aerial vehicle[37–41]. These findings provide valuable insights into the vertical

[1]College of Environment and Climate, Institute for Environmental and Climate Research, Guangdong-Hongkong-Macau Joint Laboratory of Collaborative Innovation for Environmental Quality, Jinan University, Guangzhou, China. [2]Shenzhen National Climate Observatory, Shenzhen, China. [3]Shenzhen Ecological and Environmental Monitoring Center of Guangdong Province, Shenzhen, China. ✉e-mail: lixiaobing@jnu.edu.cn; byuan@jnu.edu.cn

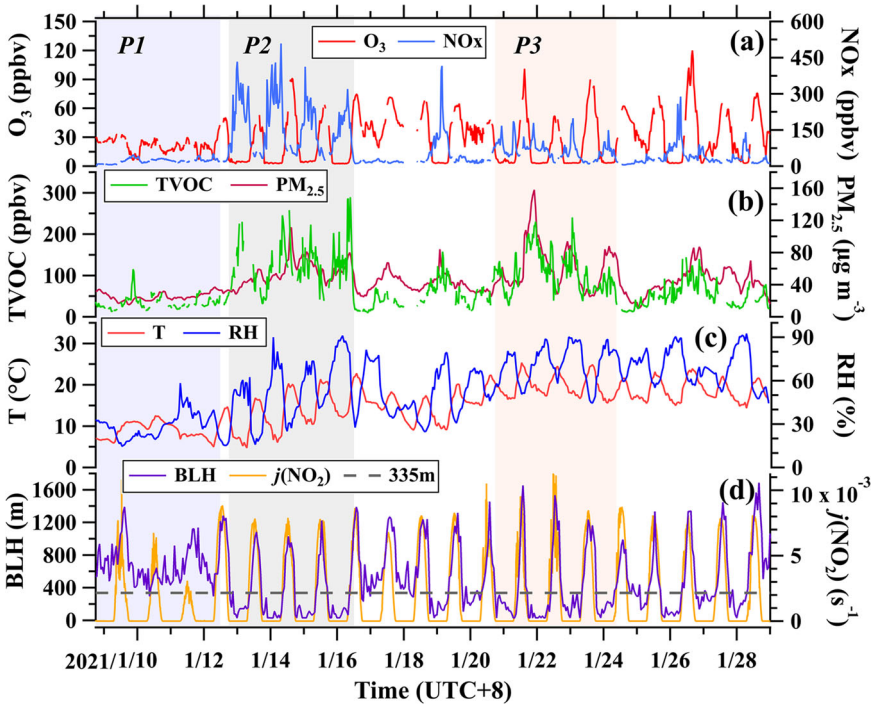

Fig. 1 | Time series of concentrations of chemical species along with meteorological parameters at ground level during the campaign. a Mixing ratios of O_3 and NOx. **b** TVOC mixing ratio and $PM_{2.5}$ concentration. **c** Temperature (T) and relative humidity (RH). **d** Boundary-layer height (BLH) and photolysis frequencies of NO_2 ($j(NO_2)$). The shaded areas indicate the three periods (P1, P2, and P3) with distinct atmospheric stabilities.

distribution patterns and sources of many VOC species within the boundary layer[42–44]. However, the temporal resolution of existing vertical VOC gradient data is highly discrete, preventing comprehensive characterization of atmospheric chemical evolution at varying altitudes throughout the day. This limitation is particularly significant in the lowest part of the troposphere (e.g., several hundreds of meters above ground level), where strong vertical VOC gradients exist[40,45]. The scarcity of continuous, high-resolution vertical VOC gradient measurements impedes a thorough examination of ozone formation chemistry in the lower troposphere.

In addition to the vertical variations in precursors, numerous studies have emphasized the substantial impact of high ozone concentrations aloft on changes in surface ozone levels[8,22,46,47]. The entrainment of ozone from above the atmospheric boundary layer, such as the free troposphere and the nocturnal residual layer, is a significant source of boundary-layer ozone. In prior research, the quantification of ozone sources has predominantly been conducted through modeling studies[48]. A limited number of investigations have utilized observed vertical ozone profiles for this quantification[8,47,49]. Nevertheless, the impact of NO titration in observation-based ozone source quantification remains inadequately explored, resulting in notable inaccuracies in determining ozone source contributions, especially in regions influenced by anthropogenic activities.

This study employed online gradient measurements of ozone and its precursor gases (NOx and a large suite of VOCs) from a meteorological tower. Using this extensive dataset, we systematically examined the vertical variations and key drivers of ozone and its precursor gases during both daytime and nighttime periods. Subsequently, the contributions of diverse sources to the daytime boundary-layer ozone budget were quantitatively evaluated using tower-based gradient measurements.

Results

Temporal and vertical variations in ozone and precursors

The hourly mean mixing ratios of surface ozone during the campaign ranged from 2.5 to 118.8 ppbv, with a mean of 28.3 ppbv, as shown in Fig. 1. Prior to January 13th, the diurnal variability of surface ozone mixing ratios was insignificant and considerably lower than that observed between January 14th and 29th. Similarly, the mixing ratios of NOx and TVOC (including 34 species listed in Table S1) and $PM_{2.5}$ concentrations before January 13th exhibited minimal diurnal variability and were significantly lower than those measured subsequently (Fig. 1). The mean air temperature and relative humidity between January 9th and 12th were 8.8 °C and 29.1%, respectively, indicating that the initial four days of the campaign were dominated by cool and dry weather conditions. Before January 13th, unstable weather conditions characterized by high boundary layer heights and large wind speeds were observed. Consequently, the low mixing ratios of ozone and its precursors before January 13th were primarily attributed to the suppression of photochemical ozone formation and favorable atmospheric dilution conditions.

After January 13th, the PRD region was affected by subsided air masses characterized by high temperatures, low relative humidity, and low wind speeds compared to the beginning of the campaign. The weather conditions were exceptionally stable, as evidenced by low boundary layer heights at night. During the campaign, the boundary layer heights lower than the maximum sampling height occurred on 11 nights. The mixing ratios of ozone and its precursors, along with $PM_{2.5}$ concentrations, at ground level were significantly enhanced with strong diurnal variability. Surface ozone at night was almost completely removed due to the presence of high NOx concentrations. Surface NOx mixing ratios were primarily composed of NO (nearly 90%, as shown in Fig. S1), with the maximum mixing ratio exceeding 300 ppbv on the nights of January 13th–16th. As a result, surface ozone was rapidly titrated by NO. Due to the strong suppression of vertical mixing in the stable nocturnal boundary layer, the mixing ratios of NOx and VOCs exhibited large vertical gradients (Fig. S2) and strong diurnal variability, with higher mixing ratios at night than during the day (Fig. 2). The enhanced accumulation of ozone precursors at night could facilitate photochemical ozone formation the following day when strong solar radiation is present (characterized by large photolysis rates of NO_2, $j(NO_2)$)[50,51].

Figure 2 shows the average diurnal variations of ozone and precursor gases (NOx and six major species measured by PTR-ToF-MS) at six different heights during the campaign. The mixing ratios of ozone at the six heights displayed unimodal diurnal variation patterns, with the maxima occurring in the early afternoon. At night, ozone and NOx mixing ratios exhibited prominent but opposite gradients from 5 m to 335 m. The average mixing ratio of ozone at 335 m (40.8 ppbv) was approximately three times larger than that at 5 m (13.5 ppbv) between 03:00 and 06:00 LT.

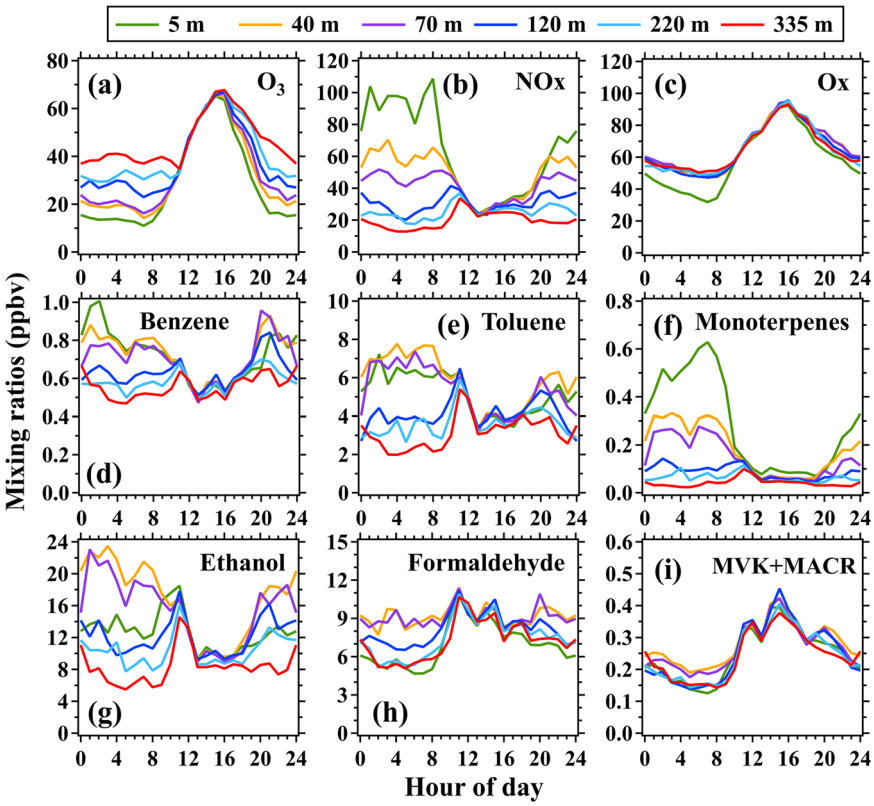

Fig. 2 | Average diurnal variations in mixing ratios of selected gaseous species at the six inlet heights during the campaign. a O_3. **b** NOx. **c** Ox. **d** Benzene. **e** Toluene. **f** Monoterpenes. **g** Ethanol. **h** Formaldehyde. **i** Methyl Vinyl Ketone and Methacrolein (MVK + MACR).

After sunrise (approximately 07:00 LT), surface ozone mixing ratios rapidly increased before reaching their maximum at 16:00 LT, then continuously declined until they reached their minimum. The mixing ratios of ozone at 335 m between 20:00 and 24:00 LT decreased more slowly than those in other heights, primarily due to the reduced effect of NO titration. The onset time of the increase in ozone was delayed from 07:00 LT at 5 m to 11:00 LT at 335 m, primarily due to the growth of the boundary layer. The Ox mixing ratio gradually increased at 335 m between 07:00 and 11:00 LT, indicating that ozone formation may occur in the aging residual layer after sunrise.

The expansion of the boundary layer can facilitate the downward entrainment of ozone from the residual layer and the upward mixing of precursor gases from surface emission sources. Between 07:00 and 08:00 LT, the mixing ratios of surface NOx peaked due to weak vertical mixing and enhanced vehicle emissions. The NOx mixing ratios measured at heights between 40 m and 335 m between 07:00 and 11:00 LT initially increased and then decreased with the growth of the boundary layer. However, surface NOx mixing ratios consistently decreased from 07:00 to 11:00 LT. The vertical exchange of air masses driven by the growth of the boundary layer will accelerate the increase of ozone in the lower part of the boundary layer and enhance photochemical ozone formation in the middle and upper boundary layers. In contrast to ozone and NOx, Ox ($O_3 + NO_2$) mixing ratios exhibited weak vertical gradients between 40 m and 335 m even during nighttime and early morning (Figs. 2 and 3), suggesting that the strong vertical gradients of ozone were mainly caused by NO titration. The lower Ox mixing ratios at ground level during nighttime could be attributed to the removal of ozone and NOx by surface dry deposition and ozone/nitrate radical (NO_3) chemistry[52,53].

The mixing ratios of three hydrocarbon species, namely benzene, toluene, and monoterpenes, exhibited temporal and vertical variation patterns similar to those of NOx during nighttime and early morning. From 8:00 to 11:00 LT, the atmospheric vertical mixing gradually increased, leading to a decrease in the concentration difference of primarily emitted species (hydrocarbon species and NOx shown in Figs. 2 and S3) across six measurement heights. After 11:00 LT, conditions for vertical mixing improved, causing the primary species' concentrations to generally decrease due to dilution and chemical removal. The accumulation of these VOCs in the stable nocturnal boundary layer indicated their continuous contributions from surface source emissions throughout the night. The rapid decline in their concentrations after 11:00 LT was primarily due to the improvement of atmospheric dilution conditions with the growth of the boundary layer and the initiation of chemical removal by hydroxyl (OH) radicals.

The average diurnal profiles of three oxygenated VOCs (OVOCs), namely ethanol, formaldehyde, and MVK + MACR, during the campaign were also presented in Fig. 2. The mixing ratios of ethanol and formaldehyde measured at six heights (see also acetone and phenol in Fig. S3) exhibited a diurnal pattern similar to that of primary species at night, suggesting their local primary emissions are also influential. The mixing ratios of formaldehyde, MVK + MACR, and cresol (Fig. S3) almost increased simultaneously at the six heights with the onset of solar irradiation, confirming the ubiquitous presence of their secondary formation throughout the boundary layer. Formaldehyde is a key intermediate oxidation product of hydrocarbons[54,55], MVK + MACR is the key oxidation product of isoprene[56], and cresol is the ring-retaining oxidation product of toluene initiated by OH radicals[57]. The diurnal variation patterns obtained at different heights indicate their mixed contributions from both secondary formation and primary emission.

Key drivers of vertical variations in ozone and its precursors

The vertical variation patterns of gaseous species in the lowest part of the troposphere are governed by a complex interplay of factors, such as surface emissions, dry and wet deposition, atmospheric dilution conditions, chemical removal and formation processes, vertical mixing, and advection transport. The vertical profiles of these gaseous species can provide valuable insights into the key factors driving their vertical change. As discussed in the above section, atmospheric stability is a crucial factor affecting the vertical variations of gaseous species at nighttime[58,59]. To further investigate the impact of atmospheric stability on the vertical variation of ozone and its

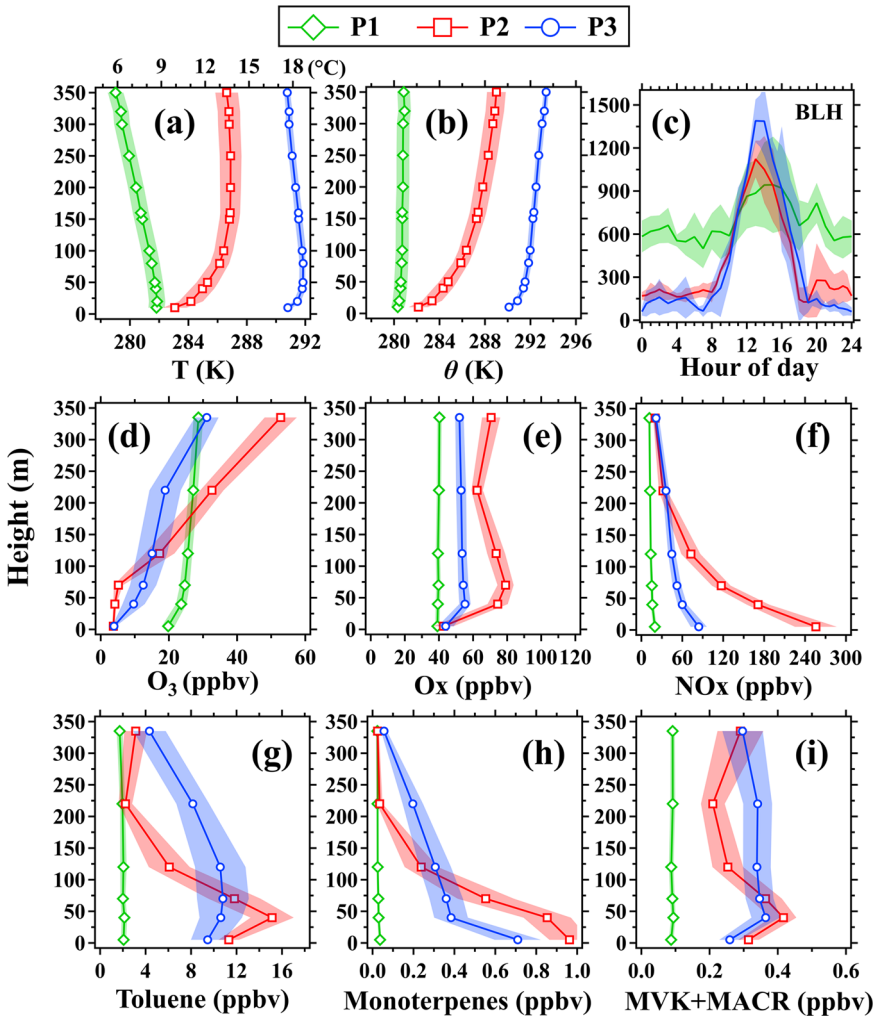

Fig. 3 | The average vertical profiles of meteorological parameters and chemical species during the three periods (P1, P2, and P3) at night (23:00–04:00 LT), as well as the diurnal variation of boundary layer height (BLH) in these three periods. **a** Temperature (T). **b** Potential temperature (θ). **d** O_3. **e** Ox. **f** NOx. **g** Toluene. **h** Monoterpenes. **i** Methyl Vinyl Ketone and Methacrolein (MVK + MACR). **c** shows average diurnal profiles of the BLH in the three periods. The shaded areas represent 30% of standard deviations.

precursors at nighttime (23:00–04:00 LT), we selected three distinct meteorological periods: period 1 (P1), period 2 (P2), and period 3 (P3), as marked in Fig. 1.

As depicted in Figs. 3 and S4, the vertical profiles of air temperature and potential temperature (θ) confirmed the presence of an unstable atmosphere below 350 m on the nighttime of P1[60]. A strong thermal inversion layer was observed on the nighttime of P2, with nocturnal boundary layer heights determined as approximately 160 m based on the change in vertical gradients of temperature profiles ($dT/dz = 0$)[61]. Additionally, strong positive gradients of θ (0.035 K m^{-1}) and relatively low wind speeds (0.5 m s^{-1}) were observed below 160 m, implying strongly stable atmospheric conditions on the nighttime of P2[60,62]. Analogous to P2, P3 was also characterized by low wind speeds at ground level, the presence of a thick thermal inversion layer, and moderate positive gradients of θ (0.0096 K m^{-1}). Therefore, atmospheric conditions in the nighttime of the three periods (namely P1, P2, and P3) were recognized as unstable, strongly stable, and moderately stable, respectively. As shown in Figs. S5–S7, there are significant disparities in the diurnal variations of chemical species across the three periods. Notably, the vertical difference escalated with an increase in atmospheric stability, particularly during nocturnal hours.

In P1, the mixing ratios of ozone, NOx, and VOCs all exhibited weak vertical gradients in the nocturnal boundary layer due to enhanced vertical mixing. However, the species profiles in P2 displayed stronger vertical gradients than those in P1 and P3. The strong atmospheric stability confined surface emissions to a thin layer above the ground. Ozone mixing ratios rapidly increased with height below 335 m, while the mixing ratios of NOx and monoterpenes rapidly declined. The average mixing ratio of NO (216.6 ppbv) in the nighttime of P2 was approximately 470 times higher than that (0.5 ppbv) in P1, due to the accumulation of surface emissions and the suppression of vertical mixing. In contrast to ozone and NOx, stratified structures were observed in vertical profiles of toluene and some OVOCs on the nighttime of P2 (Figs. 3 and S4). As introduced in "Methods" section, the tower site is located inside a protected park for a reservoir without immediately adjacent to anthropogenic emission sources. The stratified structures in vertical VOC profiles were most likely caused by the advection transport of pollution plumes from surrounding emission sources, such as vehicular exhausts. In P3, the vertical profiles of gaseous species had similar patterns to those in P2; However, the vertical gradients in P3 were weaker than those in P2.

At night, the oxidation of VOCs is primarily driven by NO_3 radicals and ozone due to the exceedingly low levels of OH radicals. The reaction rate constants of most VOC species with NO_3 radicals are substantially greater than those with ozone[63]. Consequently, the atmospheric oxidation capacity during nighttime is closely associated with the abundance and production rate of NO_3 radicals. NO_3 radicals are produced by chemical reactions of ozone with NO_2 and can be rapidly photolyzed during the day. Similar to ozone, NO_3 radical could be rapidly titrated by NO with the formation of two NO_2 molecules. Therefore, the vertical distribution of atmospheric oxidation capacity at nighttime is strongly regulated by the vertical change in concentrations of ozone and NOx[22,64]. In both P2 and P3, the nocturnal boundary layer heights were lower than 335 m (Fig. 1), providing a valuable chance to explore the factors driving

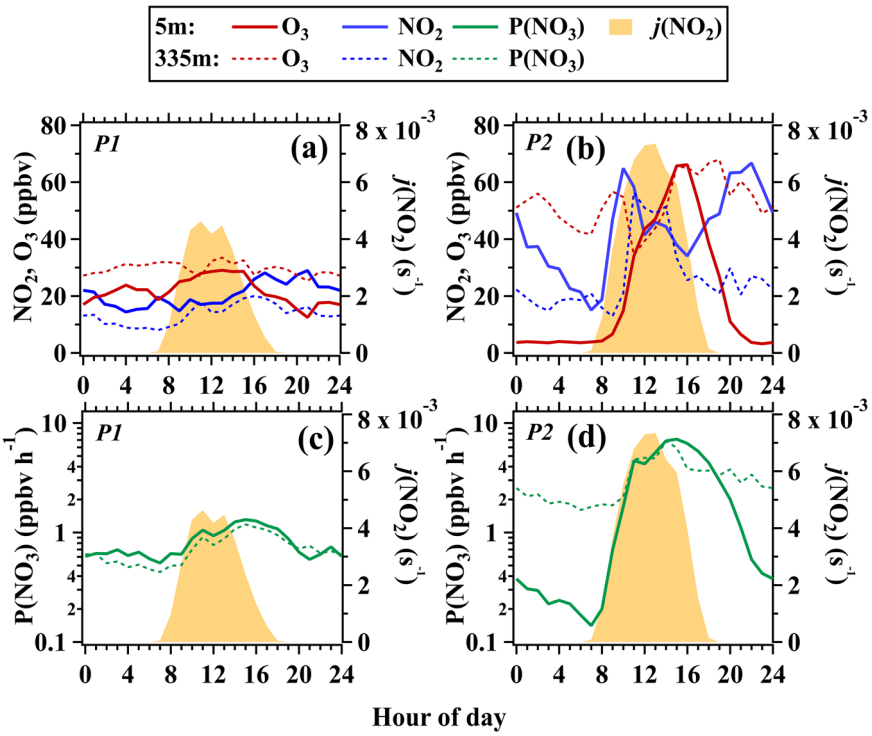

Fig. 4 | Average diurnal variations in NO_2, O_3, and the production rate of NO_3 radicals ($P(NO_3)$) at 5 and 335 m, along with photolysis frequencies of NO_2 ($j(NO_2)$) at 5 m in the strongly stable (P1) and moderately stable (P2) periods. **a** The NO_2, O_3 at 5 and 335 m, and $j(NO_2)$ at 5 m during P1. **b** The same as (**a**), but in P2. **c** The $P(NO_3)$ at 5 and 335 m, along with $j(NO_2)$ at 5 m during P1. **d** The same as (**c**), but in P2.

the change in concentrations of gaseous species in the nocturnal residual layer.

Due to the lack of direct NO_3 radical measurements, the production rate of NO_3 radicals, denoted by $P(NO_3)$, is used as an indicator to characterize the atmospheric oxidation capacity during nighttime[65]. $P(NO_3)$ was estimated used formulated in Eq. (1):

$$P(NO_3) = k_{O_3+NO_2}[O_3][NO_2] \quad (1)$$

where $k_{O_3+NO_2}$ is the reaction rate constant between ozone and NO_2 molecules; $[O_3]$ and $[NO_2]$ are the mixing ratios of ozone and NO_2, respectively. As shown in Fig. 4, the $P(NO_3)$ values during the nighttime of P1 exhibited minor differences between 5 and 335 m with an average of 0.6 ppbv h^{-1} due to the effective mixing of ozone and NOx. Conversely, the $P(NO_3)$ values at 335 m on the nighttime of P2 varied slightly with an average of 2.2 ppbv h^{-1} and were significantly greater than those (0.3 ppbv h^{-1}) at 5 m. This increase is primarily attributed to the presence of high ozone concentrations and the reduced effect of NO titration. A similar phenomenon was observed on the nighttime of P3 with moderately stable atmospheric conditions (Fig. S8). These findings provide important information that the formation potential of NO_3 radicals and the atmospheric oxidation capacity in the nocturnal residual layer is stronger than in the nocturnal boundary layer[66].

We also calculated the reactivity of VOCs and NOx with respect to NO_3[64], namely the first-order NO_3 loss constant resulting from reactions with VOCs and NOx, as denoted by NO_3 reactivity in Fig. S9. The NO_3 reactivity exhibits a wide range, spanning from less than 0.1 s^{-1} to over 100 s^{-1}. It is observed that the NO_3 reactivity during the unstable nights closely aligns with results in forested and regional sites[64,67,68], a markedly enhanced NO_3 reactivity is discerned during stable periods (P2 and P3) due to high concentrations of NO and VOCs. The results from P2 and P3 also suggest that the NO_3 reactivity gradually decreases from the surface to the residual layer, consistent with the vertical distribution patterns of NOx and reactive VOCs, such as unsaturated hydrocarbons. Considering that both ozone and $P(NO_3)$ increase with altitude during stable periods (P2 and P3), while the NO_3 reactivity decreases with increasing height, our results confirm that the atmospheric oxidation capacity in the nocturnal residual layer is stronger than that in the nocturnal boundary layer.

The amount of VOCs oxidized by ozone may represent only a minute fraction due to the abundance of NO_3 radicals in the nocturnal residual layer[69]. In the absence of significant influences from surface emissions and advection transport, the decreases in reactive VOC concentrations within the residual layer were mainly caused by chemical removal initiated by NO_3 radicals. The ratio of average mixing ratio of a VOC species, denoted by $R_{nighttime}$, between two time periods (namely 03:00–05:00 LT and 22:00–24:00 LT) in nighttime was used to characterize the change in its concentration driven by the oxidation of NO_3 radicals, as formulated in Eq. (2):

$$R_{nighttime} = [R]_{03:00-05:00\mathrm{LT}}/[R]_{22:00-24:00\mathrm{LT}} \quad (2)$$

where $[R]_{22:00\text{-}24:00\ \mathrm{LT}}$ and $[R]_{\ 03:00\text{-}05:00\ \mathrm{LT}}$ represent the average mixing ratios of the VOC species R during the two time periods, respectively. $R_{nighttime}$ can be also described using the formula of Eq. (3) if the decrease in $R_{nighttime}$ of a VOC species was dominated by reacting with NO_3 radicals.

$$R_{nighttime} = A \times \exp(-k_{NO_3-R} \times [NO_3]\Delta t) \quad (3)$$

Where k_{NO_3-R} is the rate constant for gas-phase reactions of NO_3 radicals with R. $[NO_3]\Delta t$ refers to the NO_3 radical exposure of VOCs during the period of Δt. The coefficient A was used to characterize the effect of atmospheric dilution on the change in $R_{nighttime}$.

Figure 5 illustrates the variation in $R_{nighttime}$ as a function of k_{NO_3} within the nocturnal residual layer (335 m) and at ground level (5 m) in P1 and P2, accompanied by the fitting lines derived from Eq. (3). In P1, the $R_{nighttime}$ at both 5 and 335 m generally declined with an increase in k_{NO_3}, with a more significant NO_3 radical exposure ($[NO_3]\Delta t = 5.21 \times 10^{10}$ molecules cm^{-3} s) at 5 m. Consequently, the chemical removal of VOCs by NO_3 radicals was more pronounced at the ground level than above within the nocturnal boundary layer under unstable atmospheric conditions (P1). This is attributed to the fact that during the unstable nighttime periods, ground-level ozone remains around 20 ppbv, coupled with low NO concentrations,

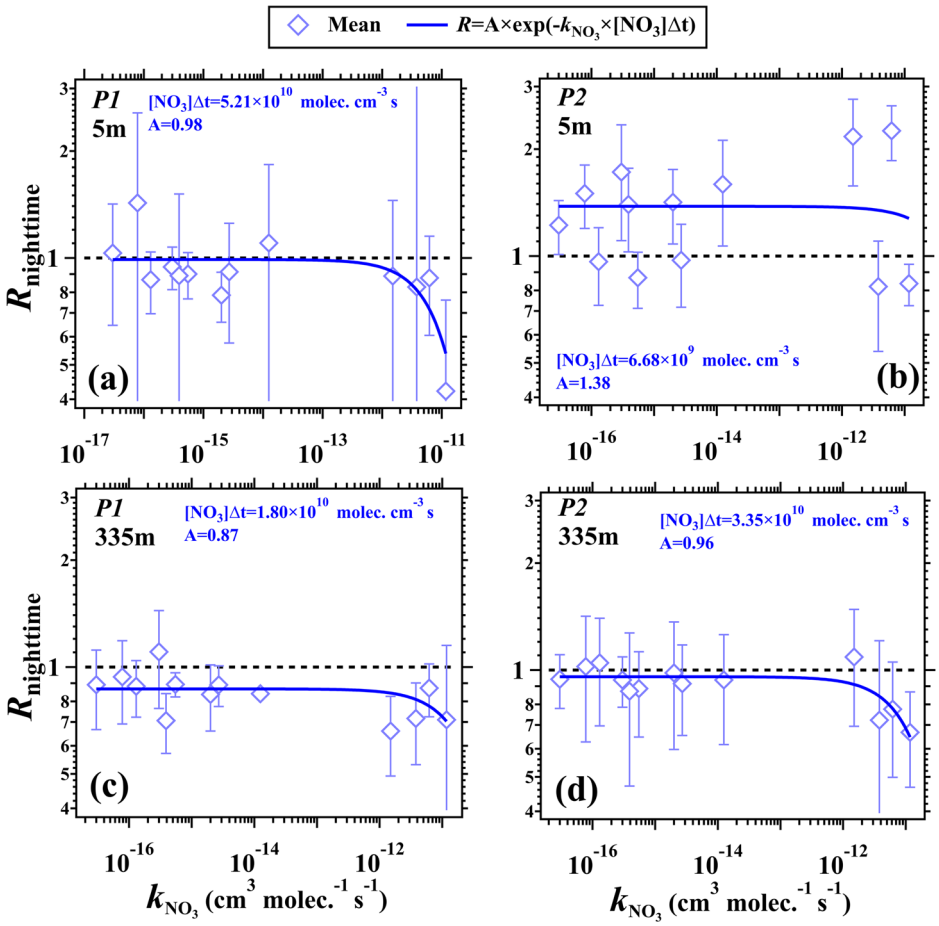

Fig. 5 | The change in $R_{nighttime}$ as a function of k_{NO3} in the strongly stable (P1) and moderately stable (P2) periods. a and **c** show the observation results at 5 m and 335 m during P1; while **b** and **d** show the observation results at the same locations during P2. $R_{nighttime}$ represents the ratio of the average species concentration in the early morning (03:00–05:00 LT) to the late evening (22:00–24:00 LT). Error bars represent standard deviations. Solid lines are fittings using the equation $R = A \times \exp(-k_{NO_3} \times [NO_3]\Delta t)$.

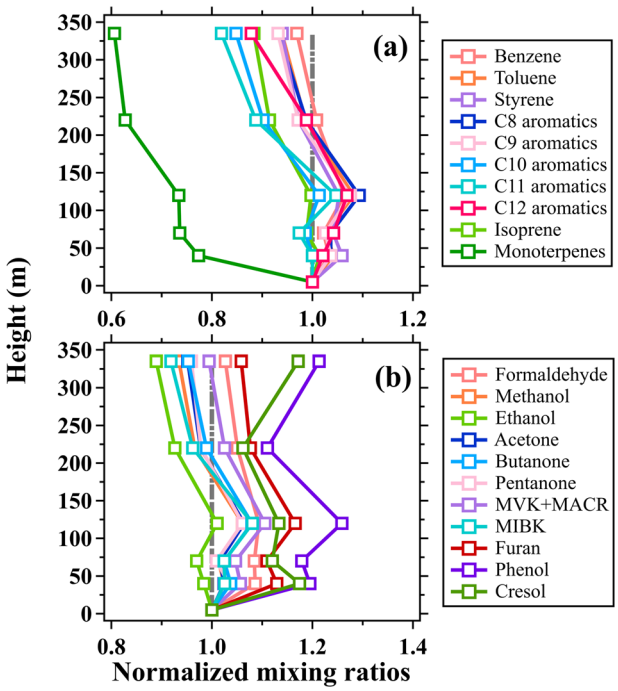

Fig. 6 | Normalized vertical profiles of the selected volatile organic compounds (VOCs) during the daytime (11:00–16:00 LT) of the campaign. a Non-methane hydrocarbons (NMHCs). **b** Oxygenated volatile organic compounds (OVOCs). The mixing ratios of VOCs measured above 5 m are normalized to those at 5 m.

creating favorable conditions for the accumulation of NO_3 (Fig. S5). In P2, the $R_{nighttime}$ obtained at 5 m shows no evidence of significant influence from NO_3 chemistry, aligning with extremely high NO concentrations. However, the $R_{nighttime}$ at 335 m significantly decreased for species with high k_{NO_3}, indicating substantial impacts of NO_3 chemistry on these reactive VOC species. These findings provide direct observational evidence confirming the existence of active chemical processes initiated by NO_3 radicals for reactive VOCs within the nocturnal residual layer. The oxidation products of these reactive species can further drive the formation of secondary organic aerosol at night and the photochemical formation of secondary gaseous pollutants for subsequent daytime periods[53].

During the day, atmospheric trace gases exhibited enhanced vertical mixing as the boundary layer expanded. Despite being significantly weaker than those in nighttime, vertical gradients of VOCs profiles were still discernible (Fig. 2). The mixing ratios of non-methane hydrocarbons (NMHCs) displayed negative but varied gradients with increasing height during the daytime (11:00–16:00 LT), as shown in Fig. 6a. Notably, monoterpenes decreased more rapidly from 5 m to 335 m compared to other species, indicating that highly reactive species such as limonene from anthropogenic sources may dominate the monoterpene composition in the study area[29]. Conversely, most OVOCs either decreased slowly or even increased with height, as shown in Fig. 6b. Atmospheric dilution had nearly the same impact on changes in concentrations of various VOCs species from the ground level to a certain height. Consequently, chemical removal/formation played a dominant role in shaping the vertical distribution patterns of VOCs in the daytime boundary layer.

NMHCs, which are primary emissions, undergo chemical consumption during the vertical mixing process along with the formation of OVOCs. In this study, the average concentration ratios of VOCs between 335 and 5 m, denoted by $R_{daytime}$ and as formulated in Eq. (4), were used to

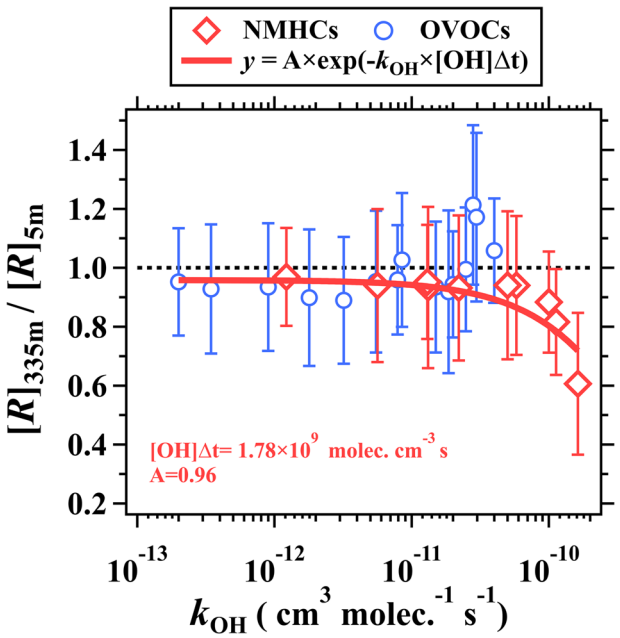

Fig. 7 | The change in $[R]_{335m}/[R]_{5m}$ as a function of k_{OH} for non-methane hydrocarbons (NMHCs) and oxygenated volatile organic compounds (OVOCs). Error bars represent standard deviations. $[R]_{335m}$ and $[R]_{5m}$ are the mean daytime mixing ratios of species at 335 m and 5 m, respectively. The red solid line is the fitting for NMHCs using the equation $y = A \times \exp(-k_{OH} \times [OH]\Delta t)$.

quantitatively characterize the vertical variation of VOCs in the daytime.

$$R_{daytime} = [R]_{335m}/[R]_{5m} \quad (4)$$

Where $[R]_{335m}$ and $[R]_{5m}$ represent the average mixing ratios of the VOC species R at 335 and 5 m, respectively. For NMHCs, $R_{daytime}$ can be also formulated as Eq. (5) if the vertical change in mixing ratios of an NMHC species was mainly driven by reacting with OH radicals[70].

$$[R]_{335m}/[R]_{5m} = A \times \exp(-k_{OH-R} \times [OH]\Delta t) \quad (5)$$

Where k_{OH-R} is the rate constant for gas-phase reactions of OH radicals with R. $[OH]\Delta t$ refers to OH radical exposure of NMHCs during the period of Δt. The coefficient A was used to characterize the effect of vertical dilution on the change in mixing ratios of NMHCs.

As shown in Fig. 7, the $R_{daytime}$ for NMHCs declines for species with higher k_{OH}, confirming the fact that the more reactive NMHCs are removed more rapidly from reaction with OH radicals. From the exponential fits of various NMHCs species, an OH exposure ($[OH]\Delta t$) at 1.98×10^9 molecules cm^{-3} s was obtained. A large value of A (0.986) indicates the minor effect of vertical dilution on the vertical change in concentrations of NMHCs between 335 m and 5 m during the daytime. The chemical removal of NMHCs during vertical mixing is accompanied by the formation of OVOCs. In addition to secondary formation, many studies suggest the important contribution of primary emissions to ambient concentrations of OVOCs[71,72]. In combination with the accumulation effect of OVOCs aloft, the $R_{daytime}$ for OVOCs exhibits insignificant dependence on the change in k_{OH}. These results further highlight the differentiated roles of atmospheric chemistry on vertical distributions of different VOC groups.

Diurnal variations in CICs of ozone and its precursors

The mixing ratios of ozone and its precursors exhibit distinct vertical gradients within the atmospheric boundary layer. Consequently, ground-level measurements of gaseous species, particularly reactive ones, are insufficient to fully characterize their total budgets (i.e., from physical and chemical sources and removal) and temporal variability throughout the entire atmospheric boundary layer. To address this issue, we utilized column-integrated concentrations (CICs) of ozone and its precursors to interpret diurnal variations of their abundances in the atmospheric boundary layer[73–75]. Here, the CICs of gaseous species were determined from the ground to the daily maximum height of the boundary layer, which corresponds to the potential top of the nocturnal residual layer (Fig. S16). The concentrations of gaseous species above 335 m were estimated using the following methods derived from their gradient measurements.

Firstly, the mixing ratios of NMHCs between 335 m and the top of the boundary layer in the daytime were estimated. As discussed in the above section, the concentration ratio of an NMHC species between two heights can be well reproduced using Eq. (5) and its reaction rate constant with OH radicals. Similarly, the mixing ratios of an NMHC species at a height (denoted as h) above 335 m within the boundary layer can be estimated using the transformation of Eq. (5). The parameters A and $[OH]\Delta t$ between 5 m and an arbitrary measurement height at a certain time can be obtained by fitting corresponding gradient measurements using Eq. (5). Then, the parameters A and $[OH]\Delta t$ between 5 m and an arbitrary height above 335 m were extrapolated based on those obtained below, as shown in Fig. S10. Consequently, for an NMHC species R, its mixing ratios at h (denoted as $[R]_h$) within the boundary layer were estimated using Eq. (6), derived from Eq. (5):

$$[R]_h = [R]_{5m} \times f_1(h) \times \exp[-k_{OH-R} \times f_2(h)] \quad (6)$$

where $f_1(h)$ and $f_2(h)$ describe the values of A and $[OH]\Delta t$ from 5 m to a specific height of h above 335 m in the boundary layer and are functions of h. k_{OH-R} is the reaction rate constant between the NMHC species R with OH radicals. In addition to NMHCs, the concentrations of NOx from 335 m to the top of the boundary layer were also estimated using Eq. (6) due to its strong reactivity with OH radicals. For other species such as Ox and OVOCs, their concentrations above 335 m within the boundary layer were assumed to be identical to those measured at 335 m.

Secondly, we estimated the mixing ratios of chemical species in the residual layer. Estimating species concentrations in the residual layer is more challenging than in the daytime boundary layer due to weak vertical mixing and complex chemical reactions. To determine the optimal method for estimating species concentrations in the residual layer, we tested three methods as discussed in "Methods" section. Finally, we considered the concentrations of chemical species in the residual layer equal to their respective mean concentrations measured at 335 m between 00:00 and 06:00 LT on the two consecutive days (Method III in "Estimation of ozone and its precursor concentrations in the residual layer" section). It should be noted that this method is only suitable for days when the nocturnal boundary layer height remains below 335 m.

Figure 8 presents the average diurnal variations in CICs and ground-level mixing ratios of selected species from January 13th to 15th. The CICs of the chemical species estimated by the other two methods are provided in Fig. S12. Compared to the mixing ratios of ozone and OVOCs at ground level, their CICs also peaked in the afternoon but exhibited weaker diurnal variability. Due to the positive vertical gradients of ozone and OVOCs, their abundances and chemical formation rates in the boundary layer may be highly underestimated using ground-level measurements. The mixing ratios of NOx and NMHCs at ground level generally exhibited typical diurnal patterns with high concentrations at night and low concentrations during the day. In contrast, the CICs of NOx and NMHCs exhibited opposite diurnal variations with apparently higher CICs during the day than at night, which is consistent with the diurnal variation patterns in their emission intensities[76]. The diurnal variations of CICs for NOx are consistent with the results derived from satellite remote-sensing data, further confirming the determined values.

Ozone precursors, primarily emitted from primary emissions at ground level, are rapidly diluted and chemically consumed as the boundary layer grows. However, the abundance of these precursors rapidly increases

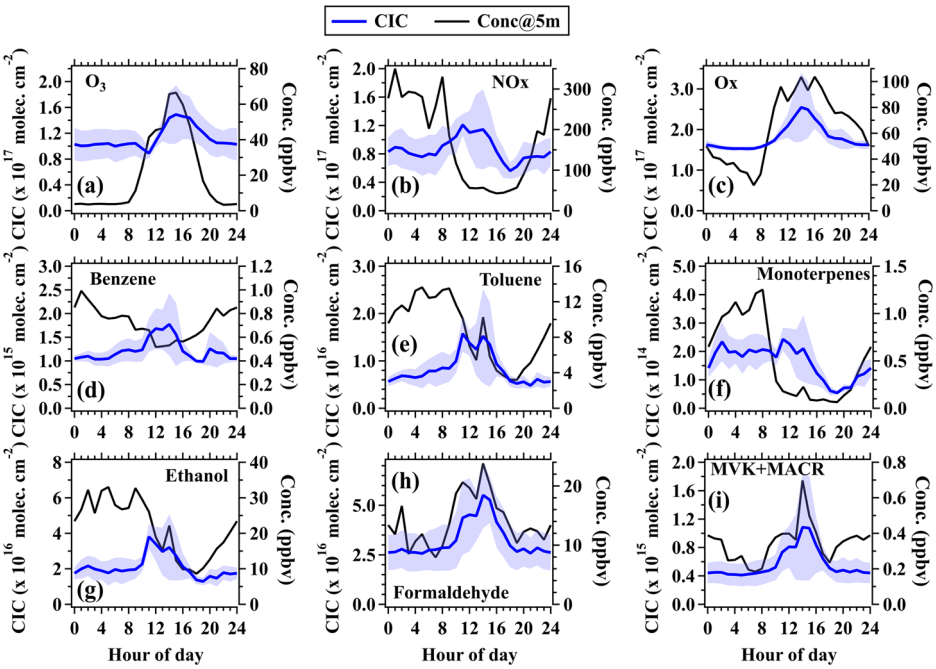

Fig. 8 | Average diurnal variations in ground-level mixing ratios and column-integrated concentrations (CICs) of selected gaseous species from January 12th to 15th. a O_3. **b** NOx. **c** Ox. **d** Benzene. **e** Toluene. **f** Monoterpenes. **g** Ethanol. **h** Formaldehyde. **i** Methyl Vinyl Ketone and Methacrolein (MVK + MACR). The shaded areas represent standard deviations.

with the growth of the boundary layer, driving photochemical ozone formation throughout the entire boundary layer. For reactive VOCs (e.g., alkenes and aromatics) that exhibit strong vertical gradients in the daytime boundary layer, their abundances in the daytime boundary layer would be overestimated if only ground-level observations were used.

The large vertical negative gradients of these reactive VOCs highlight their rapid removal by chemical reactions after being emitted from surface sources. The observed concentrations of VOCs in ambient air are the results of chemical reactions, with less reactive VOCs potentially having higher concentrations. Large discrepancies may exist in assessing the formation potentials of VOCs for ozone using ground-level observations. In this context, the use of CICs of VOCs may provide a better solution to this problem. As the boundary layer shrinks, a proportion of the primary emissions (e.g., NMHCs and NOx) and large amounts of secondarily-formed species (e.g., ozone and OVOCs) will be trapped above the boundary layer, forming the residual layer. These chemical species will then re-enter the boundary layer the following day.

Sources for the Ox increment in the daytime boundary layer

The residual layer can retain characteristics of the daytime boundary layer in the afternoon without being significantly influenced by surface fresh emissions[27,77]. The ozone-rich air masses in the residual layer can entrain into the boundary layer in the morning, contributing to the rapid increase of surface ozone[47]. The contribution of downward ozone entrainment from the residual layer to the daytime boundary layer has been quantitatively assessed in previous studies using different methods based on vertical ozone profiles[8,47,49]. In this study, we reassessed the contributions of the residual layer to the budget of the boundary-layer ozone based on changes in CICs of Ox.

In stable weather conditions, the nocturnal boundary layer heights were frequently lower than 160 m (Fig. 3c). As shown in Fig. 3d, high concentrations of ozone were observed in the residual layer on the nights of January 13th to 16th (P2, strongly stable) and January 21st to 24th (P3, moderately stable). The contributions of the three sources (namely residual layer contribution, surface emission, and chemical formation) to the increase of the boundary-layer Ox were calculated over the growth course of the boundary layer using the method described in "Methods" section (Fig. S13).

As depicted in Fig. 9, the residual layer and chemical formation were the two primary contributors to the increase of boundary-layer Ox. The contribution fractions of these three sources in the increase of boundary-layer Ox exhibited similar diurnal and day-to-day variation during the two stable periods (P2 and P3). Surface emissions accounted for small fractions in the increase of boundary-layer Ox with an average of 2.8% (09:30–13:00 LT) and decreased as the boundary layer continued to grow. The contributing fractions of chemical formation rapidly increased with the growth of the boundary layer in P2 and P3, suggesting that photochemical formation played a more significant role in elevating surface ozone levels with the enhancement of solar radiation. In P2 and P3, the average fractions of the residual layer to the increase of boundary-layer Ox gradually decreased from 71.1% to 57.0% from 09:30 to 13:00 LT, while contributions of chemical formation increased from 13.9% to 41.0%. Therefore, the downward entrainment of ozone from the residual layer was primarily responsible for the rapid increase of the boundary-layer ozone in the morning period.

The contributions of the residual layer to the boundary-layer ozone budget were estimated using a modified method based on changes in CICs of ozone, as opposed to Ox, following the methods used in Zhao et al.[49], Kaser et al.[47], and Li et al.[8]. A detailed introduction of these methods is provided in Supplementary information (Text S3.1–S3.3). In these studies[8,47,49], the contributions of the residual layer to the boundary-layer ozone during the growth course of the boundary layer were estimated based on two assumptions: (i) ozone concentrations were well mixed in the boundary layer; (ii) ozone was not substantially consumed during the vertical mixing process. The second assumption is challenging to satisfy due to the titration of ozone by NO, particularly in urban regions with strong NO emissions from vehicle exhausts. However, these assumptions may be valid for remote areas where NOx emissions from combustion sources are extremely weak.

As shown in Fig. 10a, the contribution of the residual layer (denoted by RL contribution) to the boundary-layer ozone budget was overestimated when high mixing ratios of NOx were observed at ground level. This was determined using the CICs of ozone, where Ox columns were replaced with those of ozone in Eqs. (10) and (11). In the early morning, when NOx concentrations were high (Fig. 2b), the ozone entrained from the residual layer was rapidly removed by NO, leading to the estimated RL contribution exceeding 100% based on changes in CICs of ozone. For similar reasons, the method used in Zhao et al.[49] also overestimated the contributions of the

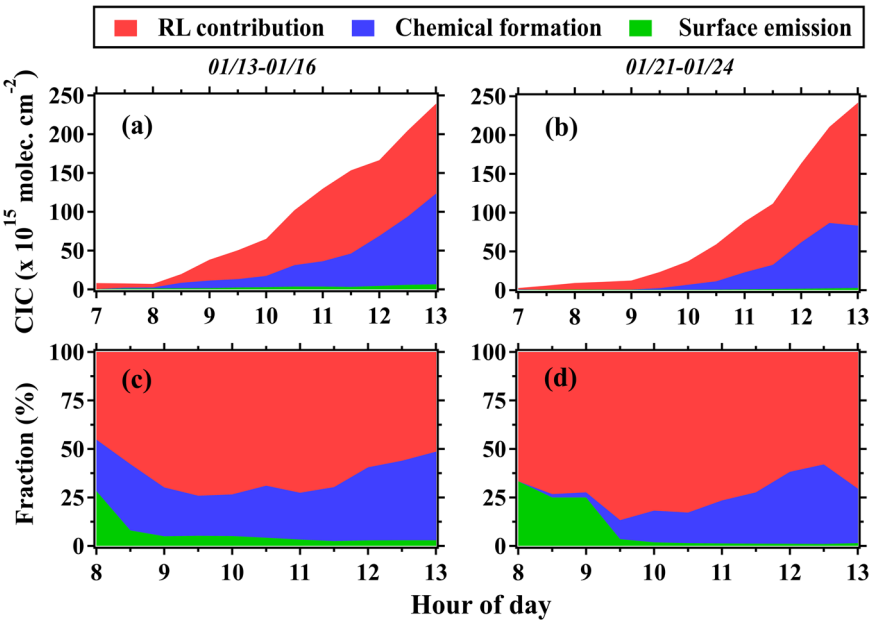

Fig. 9 | Average diurnal variations in contribution and contribution fractions of the three sources to the change in column-integrated concentrations (CICs) of Ox in the boundary layer in the strongly stable (P2) and moderately stable (P3) periods. **a** and **b** are the contribution of the three sources (namely residual layer contribution, chemical formation, and surface emission) to the change in CICs of Ox in the boundary layer in P2 and P3, respectively. **c** and **d** are the contribution fractions of the three sources to the change in CICs of Ox in the boundary layer in P2 and P3, respectively.

residual layer (marked by black crosses in Fig. S14) in the presence of high NOx concentrations. The same issue also existed in the methods used in Kaser et al.[47] and Li et al.[8], and the results are discussed in Text S3.4 of Supplementary Information.

During daytime, when NOx concentrations were low, the CICs of ozone were either equivalent to or slightly lower than those of Ox due to the reduced impact of NO titration. However, the CICs of Ox in the nighttime boundary layer remain significantly higher than those of ozone due to the pronounced effect of NO titration, as evidenced by the steep gradients of vertical ozone profiles in Fig. 3. The increase in CICs of ozone in the boundary layer between daytime and nighttime will be more substantial than that of Ox. As a result, using the CICs of ozone with low NOx concentrations may lead to an underestimation of the RL contribution, as shown in Fig. 10a.

In conclusion, the impact of NO titration must be carefully considered when assessing the contribution of various transport types to the boundary-layer ozone budget, particularly in urban areas with strong NO emissions from combustion sources. Nevertheless, vertical measurements of NOx are not always obtained due to the limitations of available techniques or platforms, such as ozone lidar and small tethered balloons. In this context, uncertainties in the RL contribution estimated using vertical ozone profiles can be approximately determined by Eq. (7) as a function of the NO_2/Ox ratio:

$$Uncertainty = \frac{RL[CIC(O_3)] - RL[CIC(O_X)]}{RL[CIC(O_X)]} 100\% \quad (7)$$

Where $RL[CIC(O_3)]$ and $RL[CIC(O_X)]$ represent the RL contribution estimated using the CICs of ozone and Ox, respectively. As shown in Fig. 10b, uncertainties of the RL contribution estimated using the CICs of ozone have a strong lognormal dependence on the change in the ratio of NO_2/Ox at the ground level. The largest mean uncertainty of 95% for the RL contribution using the CICs of ozone occurred at the NO_2/Ox ratio of approximately 0.7 and between 10:00 and 11:00 LT. A summary of the methods used in this study and previous works, as well as their improvement suggestions and application scenarios, are provided in Table S2.

Regardless of the methodological differences, all results underscore the significant contribution of ozone entrainment from the residual layer to the boundary-layer ozone budget on days with stable weather conditions. Ozone-rich air masses originating from chemical production and other sources within the daytime boundary layer can be retained in the nocturnal residual layer again if the atmosphere becomes stable at night, subsequently affecting surface ozone levels through entrainment on the following day. Therefore, the nocturnal residual layer can be viewed as a temporary reservoir for the boundary-layer ozone in the daytime. The vertical exchange of ozone between the residual and boundary layers can drive a continuous accumulation of surface ozone, leading to severe ozone pollution episodes. Separating the sources of ozone in the daytime boundary layer from those in the residual layer and photochemical formation is essential for understanding photochemical ozone formation mechanisms throughout the entire boundary layer. This understanding is critical for developing effective control strategies for ozone precursors.

Discussion

Online vertical gradient measurements of ozone and its precursors were made on a tall tower to analyze their vertical variations and key driving factors. The concentrations of ozone and its precursors exhibited vertical gradients in the boundary layer, with ozone concentrations generally increasing with height while its key precursors (e.g., NOx and NMHCs) decreasing throughout the day. During the daytime, VOCs displayed distinct vertical gradients and were significantly regulated by reactions with OH radicals. The concentrations of many OVOCs increased with height due to their secondary production during the vertical mixing process. The larger vertical concentration gradients for more reactive NMHCs implied that their observed concentrations were the result of chemical reactions, which could introduce large uncertainties in quantifying the budgets of these reactive species in the atmospheric boundary layer and assessing their potential contributions to photochemical ozone formation if only ground-level measurements were available. In this context, we proposed the use of CICs with chemical consumption correction as a promising solution to this problem.

During the nighttime, surface emissions, dry deposition, and the suppression of vertical mixing play a significant role in creating strong vertical gradients of ozone and its precursors within the nocturnal boundary layer. The observed chemistry of VOCs initiated by NO_3 radicals was more intense in the residual layer than in the boundary layer. This suggests that the nocturnal residual layer serves as a crucial place for the formation of secondary pollution. Furthermore, the entrainment of the residual layer with ozone-rich air masses could contribute to over half of the boundary-layer ozone enhancements during morning periods. These findings

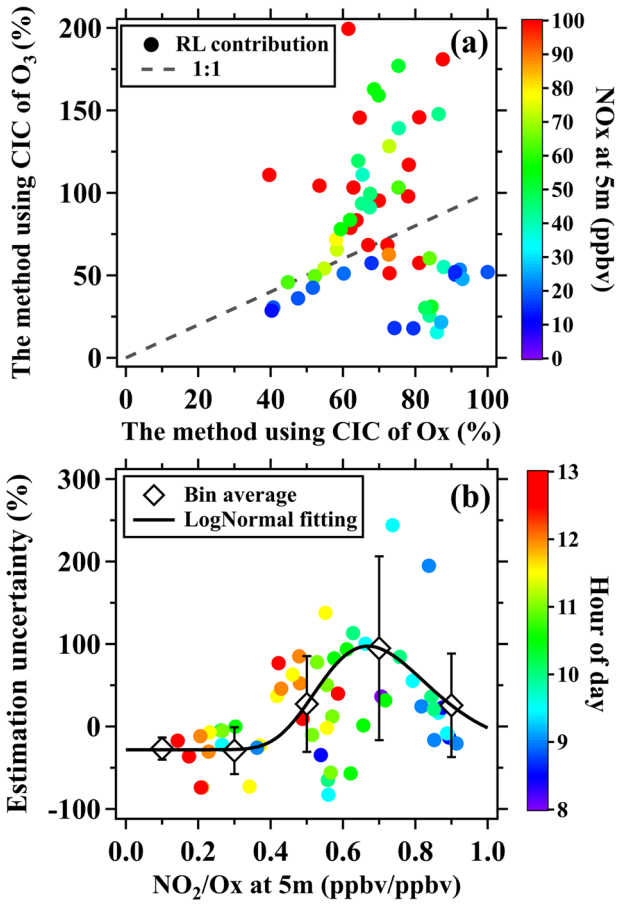

Fig. 10 | Comparison of the residual layer contribution estimated based on column-integrated concentrations (CICs) of ozone with that estimated based on CICs of Ox. a Scatter plots of the residual layer contributions to the budget of the boundary-layer ozone estimated using the method based on CICs of ozone CIC versus those estimated using the method based on CICs of Ox. **b** Uncertainty of the RL contribution estimated using the CICs of ozone as a function of the NO_2/Ox ratio.

underscore the ongoing effects of local ozone pollution and the need for precise quantification of source contributions of boundary-layer ozone.

The vertical variations in concentrations of ozone and its precursors play a crucial role in determining the changes in atmospheric chemical processes. For instance, the distinct vertical gradients of NOx and various VOCs can alter the formation rates and mechanisms of ozone at different altitudes[40,78]. Moreover, the vertical variations in concentrations of NOx and VOCs can also drive changes in the formation pathways and yields of secondary organic aerosol[79,80]. In addition to ozone, the entrainment of ozone precursors and the oxidation products of VOCs from the residual layer can significantly impact the formation of ozone in the daytime boundary layer the following day[52,53]. Therefore, further investigation is needed to understand the vertical changes in atmospheric chemistry and their related environmental impacts.

Methods

Site description and field campaign

Vertical gradient measurements of ozone and its precursors, namely VOCs and NOx ($NO + NO_2$), were conducted on the Shiyan Meteorology Tower (SMT) in Shenzhen, China. The SMT has a height of 356 m and is located inside a protected park for water in the western suburban Shenzhen and the eastern part of the Pearl River Delta (PRD) region[81]. PRD is one of the most developed, populated, and industrialized regions in China and also faces serious secondary air pollution problems[82]. Despite continuous reductions in anthropogenic emissions, surface ozone concentrations have shown rising trends over the urban areas of PRD in the recent two decades[12]. Therefore, the abatement of ozone pollution has been the key to the improvement of regional air quality in PRD.

The surrounding land-use types of the SMT site primarily consist of water, evergreen arbor, industrial parks, residential buildings, freeways, and an airport. The SMT is situated approximately 20 km northwest of downtown Shenzhen and 10 km west of the Shenzhen Bao'an International Airport. A three-lane expressway in both directions is located about 1 km to the north and northeast of the SMT. Several industrial parks are situated about 2 km to the north of the SMT. Consequently, atmospheric composition concentrations at the SMT site are influenced by a complex array of emission sources. Detailed descriptions of the SMT have been provided in other literature[81,83]. The field campaign was conducted from January 8th to 29th, 2021.

Instrumentation and data acquisition

Meteorological parameters, including air temperature (T), relative humidity (RH), air pressure, wind speed, and wind direction, were directly measured at 13 heights ranging from 10 to 350 m on the tower. Online gradient measurements of ozone and its precursors were made using a tower-based observation system that features five inlet heights (40 m, 70 m, 120 m, 220 m, and 335 m) on the tower. Besides, an additional sampling inlet was mounted on the rooftop of the observation room (approximately 5 m above ground level) at the SMT base. A detailed description and assessment of the vertical observation system have been provided in our previous study, and a brief description is provided here.

Two PFA-Teflon tubes (OD: 1/2") were installed at each sampling height, with one for backup. The inlet end of the tubing on the tower was connected to a filter to remove fine particles. A vacuum pump was used to simultaneously draw air samples from the six tubes. The flow rate of the sample gas stream in each tubing was controlled by a critical orifice. Subsamples were sequentially drawn by instruments from the six tubes through a solenoid valve group that can perform the switch of the sampling heights at adjustable time intervals. In this study, the switching time intervals between inlet heights were set as 2 min, thus requiring 12 min to complete a full vertical profile measurement. All the instruments were operated in an air-conditioned room at the SMT base.

VOC measurements were made by a proton transfer reaction time-of-flight mass spectrometry (PTR-QiToF-MS, IONICON Analytik, Innsbruck, Austria) with time resolutions of 5 s. The PTR-ToF-MS operated at an E/N ratio of approximately 120 Td. The raw mass spectral data were processed using high-resolution peak fittings in Tofware (Tofwerk AG, v3.0.3). The PTR-ToF-MS has both H_3O^+ [27,84,85] and NO^+ [86,87] ion sources, which can be automatically switched at designated time intervals. During the campaign, the PTR-ToF-MS was operated in the H_3O^+ mode for the first 44 min of one hour and in the NO^+ mode for the last 16 min. Blank measurements were automatically taken for 2 min before the switch of the ion source by passing ambient air through a platinum catalyst (heated to 365 °C to remove VOCs). A certified gas standard containing 34 VOC species (Table S1) was used to calibrate the instrument three times daily for the H_3O^+ mode[27]. Effects of ambient humidity on measured ion signals were eliminated using humidity dependence curves of the VOC species determined in our laboratory after the field campaign[85,86].

A CO_2/H_2O gas analyzer (Li-840A, Licor Inc., USA) was employed to measure ambient humidity at time resolutions of 5 s. Ozone and NOx measurements were made at time resolutions of 10 s using the ultraviolet photometry method (49i, Thermo Fisher Scientific Inc., USA) and the chemiluminescence method (42i, Thermo Fisher Scientific Inc., USA), respectively. $PM_{2.5}$ concentrations at ground level were obtained from an automated monitoring station at the SMT base operated by the Shenzhen Ecological and Environmental Monitoring Center of Guangdong Province[81]. Boundary-layer height (BLH) at the tower site was obtained from simulation results of the Weather Research and Forecasting model (WRF v4.1.2)[88]. Additionally, nocturnal boundary layer heights were corrected using the vertical gradients of temperature measured by the tower platforms.

Source analysis of ozone in the daytime boundary layer

Based on the gradient measurements of Ox ($O_3 + NO_2$) and NOx, we proposed a new approach to estimate the contributions of downward entrainment and chemical formation to the boundary-layer ozone budget during the growth process of the atmospheric boundary layer. Unlike previous studies, this approach was developed based on changes in columns of Ox and NOx, denoted by column-integrated concentrations (CICs), in both the boundary layer and the nocturnal residual layer, rather than relying solely on vertical ozone measurements.

Ox is a more reliable metric for characterizing the spatio-temporal changes of ozone by eliminating the impacts from NO titration[12]. This approach does not incorporate contributions from advection ozone transport, which is reasonable given that the nocturnal residual layer was well-formed in stable weather conditions when the advection transport of air pollutants from adjacent regions is weak. The CICs of a gaseous species *i* are calculated using the method formulated in Eq. (8),

$$CIC_{layer}(i)_t = \int_{h1}^{h2} [i]_h \frac{N_A}{V_{molar}(h)} dh \tag{8}$$

where $CIC_{layer}(i)_t$ represents the CIC of the species *i* within an air layer (e.g., the nocturnal boundary layer (NBL), the residual layer (RL), and the boundary layer (BL)) at time *t* (*unit: molecules* cm^{-2}). $[i]_h$ represents the volume mixing ratio (parts per billion in volume, ppbv) of the species *i* at an altitude *h* (*unit:* 10^{-9} *mol* mol^{-1}). h_1 and h_2 represent the lowest and the highest altitudes of the air layer, respectively (*unit: cm*). The Avogadro constant is denoted as N_A (6.02×10^{23} *molecules* mol^{-1}). V_{molar} *(h)* is the molar volume of gas (*unit:* cm^3 mol^{-1}) as a function of *h* due to the vertical change in air temperature (*unit: K*) and air pressure (*unit: hPa*).

The gradient measurements of gaseous species were insufficient to fully characterize the daytime boundary layer due to the limited height of the tower. Under these conditions, the approach described above was established based on the following assumptions: (i) The residual layer height was estimated to be the maximum height of the daytime boundary layer from the previous day (Fig. S16); (ii) The linear interpolation method was used to estimate concentrations of gaseous species between two inlet heights; (iii) Concentrations of gaseous species below 5 m were assigned to those at 5 m; (iv) The concentrations between the maximum measurement height (335 m) and the top of the residual layer or the top of the boundary layer can be estimated based on our observations. This assumption was proposed based on our observations and has been discussed in "Diurnal variations in CICs of ozone and its precursors" section and Supplementary Information.

The change in the CIC of Ox in the daytime boundary layer can be ascribed to three major sources: downward entrainment from the nocturnal residual layer, net chemical formation, and surface emission (Fig. S17, Eq. (9)).

$$\Delta CIC_{BL}(Ox)_t = C_{RL}(Ox)_t + C_E(Ox)_t + C_{CF}(Ox)_t \tag{9}$$

Where $\Delta CIC_{BL}(Ox)_t$ represents the change in $CIC_{BL}(Ox)$ at time *t* relative to its mean value in nighttime. The mean value during nighttime was calculated between 03:00 and 05:00 local time (LT, UTC + 8), as air masses varied minimally during this period (Fig. S18) when influenced by stable weather conditions. $C_{RL}(Ox)_t$ denotes the contribution of Ox from the nocturnal residual layer, $C_{CF}(Ox)_t$ denotes the contribution of Ox from net chemical formation, and $C_E(Ox)_t$ indicates the contribution of Ox from surface emissions (*unit: molecule* cm^{-2}).

The left term of Eq. (9) can be determined by:

$$\Delta CIC_{BL}(Ox)_t = \int_0^{BLH_t} [Ox]_{t,h} \frac{N_A}{V_{molar\,t,h}} dh - \int_0^{BLH_{night}} [Ox]_{night,h} \frac{N_A}{V_{molar\,night,h}} dh \tag{10}$$

where $[Ox]_{t,h}$ signifies the mixing ratio of Ox at time t and altitude h. BLH_t and BLH_{night} indicate the heights of the boundary layer at time t and during nighttime (03:00–05:00 LT), respectively.

The first term on the right in the Eq. (9)

$$C_{RL}(Ox)_t = \int_{BLH_{night}}^{RLH_{night}} [Ox]_{night,h} \frac{N_A}{V_{molar\,night,h}} dh - \int_{BLH_t}^{RLH_t} [Ox]_{t,h} \frac{N_A}{V_{molar\,t,h}} dh \tag{11}$$

where RLH_t and RLH_{night} denote the heights of the residual layer at time *t* and in nighttime (03:00–05:00 LT), respectively.

The second term on the right in Eq. (9) $C_E(Ox)_t$ indicates the contribution of Ox from surface emissions, which is contributed by primary NO_2 emissions. This can be expressed mathematically as in Eq. (12):

$$C_E(Ox)_t = \left[\int_0^{RLH_t} [NOx]_{t,h} \frac{N_A}{V_{molar\,t,h}} dh - \int_0^{RLH_{night}} [NOx]_{night,h} \frac{N_A}{V_{molar\,night,h}} dh \right] \times ER \tag{12}$$

where $[NOx]_{t,h}$ is the mixing ratio of NOx at time *t* and altitude *h*. ER (*unit: ppbv* $ppbv^{-1}$) denotes the primary emission ratios of NO_2 relative to NOx from combustion sources. Apart from on-road traffic emissions, there are no other significant NOx sources in the vicinity of the SMT site. Based on our measurements (Fig. S1), ER is set as 10%, which aligns well with the reported emission characteristics of on-road vehicles in the literature[89,90].

The third right term in Eq. (9) $C_{CF}(Ox)_t$, as the chemical formation contribution, is equal to the change in total CIC of Ox at time *t* compared to nighttime and deduction of surface emissions:

$$C_{CF}(Ox)_t = \left[\int_0^{RLH_t} [Ox]_{t,h} \frac{N_A}{V_{molar\,t,h}} dh - \int_0^{RLH_{night}} [Ox]_{night,h} \frac{N_A}{V_{molar\,night,h}} dh \right] - C_E(Ox)_t \tag{13}$$

The sum of the calculation results of the right terms in Eqs. (11)–(13) is equivalent to the result on the right side of Eq. (10), thus completing the closed loop of the calculation (Eq. 14). By utilizing Eqs. (8)–(13), we can compute $\Delta CIC_{BL}(Ox)_t$ and its contributions from three factors, namely ($C_{RL}(Ox)_t$, $C_{CF}(Ox)_t$, and $C_E(Ox)_t$) can be calculated.

$$\begin{aligned} &C_{RL}(Ox)_t + C_{CF}(Ox)_t + C_E(Ox)_t \\ &= \left\{ CIC_{RL}(Ox)_{night} - CIC_{RL}(Ox)_t \right\} \\ &+ \left\{ \left[CIC_{BL+RL}(Ox)_t - CIC_{NBL+RL}(Ox)_{night} \right] - C_E(Ox)_t \right\} + C_E(Ox)_t \\ &= CIC_{RL}(Ox)_{night} - CIC_{NBL+RL}(Ox)_{night} + CIC_{BL+RL}(Ox)_t - CIC_{RL}(Ox)_t \\ &= CIC_{BL}(Ox)_t - CIC_{BL}(Ox)_{night} \\ &= \Delta CIC_{BL}(Ox)_t \end{aligned} \tag{14}$$

Estimation of ozone and its precursor concentrations in the residual layer

As the boundary layer shrinks, a proportion of the primary emissions (e.g., NMHCs and NOx) and large amounts of secondarily-formed species (e.g., ozone and OVOCs) will be trapped above the boundary layer, forming the residual layer. The concentrations of chemical species in the boundary layer (BL) can be estimated using the gradient measurements. However, estimating concentrations of these species between above the BL and the top of the residual layer presents significant challenges due to the tower's limited height and the restricted air mass exchange. In this study, we proposed and discussed three methods based on our gradient measurements to estimate

the concentrations of NOx and VOCs in the residual layer. The results of these three methods for toluene and acetaldehyde are displayed in Fig. S11.

Method I

As discussed in "Diurnal variations in CICs of ozone and its precursors" section and illustrated in Fig. S17, the residual layer formed as a result of the decrease in BL height of BL until the BL reached the same height the following day. Consequently, concentrations of a species at a specific height above the BL and the maximum measurement height (335 m) were deemed equivalent to its concentration when the BL height decreased to this level. Furthermore, concentrations of the species at a given height in the residual layer remained constant until the BL ascended to this height the subsequent day. In this approach, concentrations of the species in the residual layer exhibited significant vertical gradients yet remained consistent over time.

Method II

At any given moment, the concentrations of a species above the BL and the maximum measurement height (335 m) were considered equivalent to its concentration at 335 m. This method presumes that concentrations of the species within the residual layer exhibited no vertical gradients, yet they varied over time.

Method III

During stable weather conditions, the height of the nocturnal boundary layer typically remained below 335 m. The concentrations of the species measured at 335 m could represent, to some extent, the actual state of the residual layer. Consequently, the concentrations of a species above the BL and the maximum measurement height (335 m) at any given height and time were considered equivalent to its average concentration measured at 335 m between 00:00 and 06:00 LT. Using this method, concentrations of the species in the residual layer exhibited no vertical gradients and remained constant over time.

Figure S12 shows average diurnal variations in CICs of the selected species during the P2 period (January 12th to 15th) as estimated by the three methods. Due to the lack of measurements, the actual concentrations of the species in the residual layer were unknown. All three methods discussed above presented unexpected uncertainties in estimating the CICs of the species. Method I may have overestimated CICs of all species, as chemical removal of species above the boundary layer is also possible, particularly during the day. Method II may have overestimated CICs of NMHCs and NOx while underestimating some OVOCs, since concentrations of NMHCs and NOx generally decreased with height in the BL. As for the OVOCs from secondary formation, their concentrations generally increased with height in the BL. Method III serves as a compromise compared to Methods I and II. The diurnal changes in CICs of NOx derived from Method III aligned more closely with satellite-based remote-sensing data compared to the other two methods[91]. Therefore, CICs of the species derived from Method III were primarily used in this study.

Data availability

The datasets used and/or analyzed during the current study are available from the corresponding author upon reasonable request.

Received: 7 May 2024; Accepted: 21 October 2024;
Published online: 28 October 2024

References

1. Ding, A. J. et al. Intense atmospheric pollution modifies weather: a case of mixed biomass burning with fossil fuel combustion pollution in eastern China. *Atmos. Chem. Phys.* **13**, 10545–10554 (2013).
2. Ma, M. et al. Substantial ozone enhancement over the North China Plain from increased biogenic emissions due to heat waves and land cover in summer 2017. *Atmos. Chem. Phys.* **19**, 12195–12207 (2019).
3. Chen, T. et al. Volatile organic compounds and ozone air pollution in an oil production region in northern China. *Atmos. Chem. Phys.* **20**, 7069–7086 (2020).
4. Li, K. et al. Increases in surface ozone pollution in China from 2013 to 2019: anthropogenic and meteorological influences. *Atmos. Chem. Phys.* **20**, 11423–11433 (2020).
5. Perdigones, B. C., Lee, S., Cohen, R. C., Park, J.-H. & Min, K.-E. Two decades of changes in summertime ozone production in California's South Coast Air Basin. *Environ. Sci. Technol.* **56**, 10586–10595 (2022).
6. Gaudel, A. et al. Aircraft observations since the 1990s reveal increases of tropospheric ozone at multiple locations across the Northern Hemisphere. *Sci. Adv.* **6**, eaba8272 (2020).
7. Zhang, X. et al. Discrepancies in ozone levels and temporal variations between urban and rural North China Plain: Possible implications for agricultural impact assessment across China. *Elementa Sci. Anthr.* **10**, 819 (2022).
8. Li, X. B. & Fan, G. Interannual variations, sources, and health impacts of the springtime ozone in Shanghai. *Environ. Pollut.* **306**, 119458 (2022).
9. Ou, J. et al. Ambient ozone control in a photochemically active region: short-term despiking or long-term attainment? *Environ. Sci. Technol.* **50**, 5720–5728 (2016).
10. Chen, Z. et al. Understanding long-term variations of meteorological influences on ground ozone concentrations in Beijing During 2006-2016. *Environ. Pollut.* **245**, 29–37 (2019).
11. Sun, Y. et al. The drivers and health risks of unexpected surface ozone enhancements over the Sichuan Basin, China, in 2020. *Atmos. Chem. Phys.* **21**, 18589–18608 (2021).
12. Li, X.-B. et al. Long-term trend of ozone in southern China reveals future mitigation strategy for air pollution. *Atmos. Environ.* https://doi.org/10.1016/j.atmosenv.2021.118869 (2022).
13. Yu, S. et al. Characterization of ambient volatile organic compounds, source apportionment, and the ozone-NOx-VOC sensitivities in a heavily polluted megacity of central China: effect of sporting events and emission reductions. *Atmos. Chem. Phys.* **21**, 15239–15257 (2021).
14. Zhang, Y. et al. Development of ozone reactivity scales for volatile organic compounds in a Chinese megacity. *Atmos. Chem. Phys.* **21**, 11053–11068 (2021).
15. Qu, H. et al. Chemical production of oxygenated volatile organic compounds strongly enhances boundary-layer oxidation chemistry and ozone production. *Environ. Sci. Technol.* **55**, 13718–13727 (2021).
16. Chen, L. et al. Vertical profiles of O_3, NO_2 and PM in a major fine chemical industry park in the Yangtze River Delta of China detected by a sensor package on an unmanned aerial vehicle. *Sci. Total Environ.* **845**, 157113 (2022).
17. Dieu Hien, V. T. et al. An overview of the development of vertical sampling technologies for ambient volatile organic compounds (VOCs). *J. Environ. Manag.* **247**, 401–412 (2019).
18. Aneja, V. P. et al. Coupling the vertical distribution of ozone in the atmospheric boundary layer. *Environ. Sci. Technol.* **34**, 2324–2329 (2000).
19. Ding, A. J., Wang, T., Thouret, V., Cammas, J. P. & Nédélec, P. Tropospheric ozone climatology over Beijing: analysis of aircraft data from the MOZAIC program. *Atmos. Chem. Phys.* **8**, 1–13 (2008).
20. Huang, X. et al. Chemical boundary layer and its impact on air pollution in Northern China. *Environ. Sci. Technol. Lett.* **7**, 826–832 (2020).
21. Pfannerstill, E. Y. et al. Total OH reactivity over the Amazon rainforest: variability with temperature, wind, rain, altitude, time of day, season, and an overall budget closure. *Atmos. Chem. Phys.* **21**, 6231–6256 (2021).

22. Caputi, D. J. et al. Residual layer ozone, mixing, and the nocturnal jet in California's San Joaquin Valley. *Atmos. Chem. Phys.* **19**, 4721–4740 (2019).
23. Tang, G. et al. Aggravated ozone pollution in the strong free convection boundary layer. *Sci. Total Environ.* **788**, 147740 (2021).
24. Pisano, J. T., McKendry, I., Steyn, D. G. & Hastie, D. R. Vertical nitrogen dioxide and ozone concentrations measured from a tethered balloon in the Lower Fraser Valley. *Atmos. Environ.* **31**, 2071–2078 (1997).
25. Li, X.-B. et al. Three-dimensional analysis of ozone and $PM_{2.5}$ distributions obtained by observations of tethered balloon and unmanned aerial vehicle in Shanghai, China. *Stoch. Environ. Res. Risk Assess.* **32**, 1189–1203 (2018).
26. Li, X.-B. et al. Three-dimensional investigation of ozone pollution in the lower troposphere using an unmanned aerial vehicle platform. *Environ. Pollut.* **224**, 107–116 (2017).
27. Li, X.-B. et al. Variations and sources of volatile organic compounds (VOCs) in urban region: insights from measurements on a tall tower. *Atmos. Chem. Phys.* **22**, 10567–10587 (2022).
28. Atkinson, R. & Arey, J. Atmospheric degradation of volatile organic compounds. *Chem. Rev.* **103**, 4605–4638 (2003).
29. Gkatzelis, G. I. et al. Observations confirm that volatile chemical products are a major source of petrochemical emissions in U.S. cities. *Environ. Sci. Technol.* **55**, 4332–4343 (2021).
30. Ting, M., Yue-si, W., Jie, J., Fang-kun, W. & Mingxing, W. The vertical distributions of VOCs in the atmosphere of Beijing in autumn. *Sci. Total Environ.* **390**, 97–108 (2008).
31. Sangiorgi, G. et al. Vertical distribution of hydrocarbons in the low troposphere below and above the mixing height: tethered balloon measurements in Milan, Italy. *Environ. Pollut.* **159**, 3545–3552 (2011).
32. Yáñez-Serrano, A. M. et al. Diel and seasonal changes of biogenic volatile organic compounds within and above an Amazonian rainforest. *Atmos. Chem. Phys.* **15**, 3359–3378 (2015).
33. Zhao, W. et al. Vertical distribution of particle-phase dicarboxylic acids, oxoacids and α-dicarbonyls in the urban boundary layer based on the 325 m tower in Beijing. *Atmos. Chem. Phys.* **20**, 10331–10350 (2020).
34. Blanchard, C. L. Ozone process insights from field experiments – Part III: extent of reaction and ozone formation. *Atmos. Environ.* **34**, 2035–2043 (2000).
35. Lu, Y. et al. Characteristics and sources analysis of ambient volatile organic compounds in a typical industrial park: Implications for ozone formation in 2022 Asian Games. *Sci. Total Environ.* **848**, 157746 (2022).
36. Ou, J. et al. Speciated OVOC and VOC emission inventories and their implications for reactivity-based ozone control strategy in the Pearl River Delta region, China. *Sci. Total Environ.* **530-531**, 393–402 (2015).
37. Mo, Z. et al. Tower-based measurements of NMHCs and OVOCs in the Pearl River Delta: vertical distribution, source analysis and chemical reactivity. *Environ. Pollut.* **292**, 118454 (2022).
38. Velasco, E. et al. Vertical distribution of ozone and VOCs in the low boundary layer of Mexico City. *Atmos. Chem. Phys.* **8**, 3061–3079 (2008).
39. Zhang, K. et al. Vertical distribution of volatile organic compounds within the lower troposphere in late spring of Shanghai. *Atmos. Environ.* **186**, 150–157 (2018).
40. Benish, S. E. et al. Measurement report: Aircraft observations of ozone, nitrogen oxides, and volatile organic compounds over Hebei Province, China. *Atmos. Chem. Phys.* **20**, 14523–14545 (2020).
41. Vo, T.-D.-H. et al. Vertical stratification of volatile organic compounds and their photochemical product formation potential in an industrial urban area. *J. Environ. Manag.* **217**, 327–336 (2018).
42. Wu, S. et al. Vertical evolution of boundary layer volatile organic compounds in summer over the North China Plain and the differences with winter. *Adv. Atmos. Sci.* **38**, 1165–1176 (2021).
43. Liu, Y. et al. Vertical profiles of volatile organic compounds in suburban Shanghai. *Adv. Atmos. Sci.* **38**, 1177–1187 (2021).
44. Sun, J. et al. Vertical characteristics of VOCs in the lower troposphere over the North China Plain during pollution periods. *Environ. Pollut.* **236**, 907–915 (2018).
45. Mo, Z. et al. Deriving emission fluxes of volatile organic compounds from tower observation in the Pearl River Delta, China. *Sci. Total Environ.* **741**, 139763 (2020).
46. Haman, C. L. et al. Relationship between boundary layer heights and growth rates with ground-level ozone in Houston, Texas. *J. Geophys. Res.: Atmos.* **119**, 6230–6245 (2014).
47. Kaser, L. et al. The effect of entrainment through atmospheric boundary layer growth on observed and modeled surface ozone in the Colorado Front Range. *J. Geophys. Res.: Atmos.* **122**, 6075–6093 (2017).
48. Lu, X. et al. Exploring 2016–2017 surface ozone pollution over China: source contributions and meteorological influences. *Atmos. Chem. Phys.* **19**, 8339–8361 (2019).
49. Zhao, W. et al. Evolution of boundary layer ozone in Shijiazhuang, a suburban site on the North China Plain. *J. Environ. Sci.* **83**, 152–160 (2019).
50. Wang, S., Ackermann, R. & Stutz, J. Vertical profiles of O_3 and NOx chemistry in the polluted nocturnal boundary layer in Phoenix, AZ: I. Field observations by long-path DOAS. *Atmos. Chem. Phys.* **6**, 2671–2693 (2006).
51. Mathur, R. et al. A call for an aloft air quality monitoring network: Need, feasibility, and potential value. *Environ. Sci. Technol.* **52**, 10903–10908 (2018).
52. Edwards, P. M. et al. Transition from high- to low-NOx control of night-time oxidation in the southeastern US. *Nat. Geosci.* **10**, 490–496 (2017).
53. Millet, D. B. et al. Nighttime chemistry and morning isoprene can drive urban ozone downwind of a major deciduous forest. *Environ. Sci. Technol.* **50**, 4335–4342 (2016).
54. Liu, L. et al. A photochemical modeling study of ozone and formaldehyde generation and budget in the Po basin. *J. Geophys. Res.* https://doi.org/10.1029/2006jd008172 (2007).
55. Anderson, D. C. et al. Formaldehyde in the tropical western pacific: chemical sources and sinks, convective transport, and representation in CAM-Chem and the CCMI models. *J. Geophys. Res.: Atmos.* **122**, 11201–11226 (2017).
56. Zhang, X. et al. Probing isoprene photochemistry at atmospherically relevant nitric oxide levels. *Chem* https://doi.org/10.1016/j.chempr.2022.08.003 (2022).
57. Schwantes, R. H. et al. Formation of highly oxygenated low-volatility products from cresol oxidation. *Atmos. Chem. Phys.* **17**, 3453–3474 (2017).
58. Glaser, K. Vertical profiles of O_3, NO_2, NOx, VOC, and meteorological parameters during the Berlin Ozone Experiment (BERLIOZ) campaign. *J. Geophys. Res.* https://doi.org/10.1029/2002jd002475 (2003).
59. Cesler-Maloney, M. et al. Differences in ozone and particulate matter between ground level and 20 m aloft are frequent during wintertime surface-based temperature inversions in Fairbanks, Alaska. *J. Geophys. Res. Atmos.* https://doi.org/10.1029/2021jd036215 (2022).
60. Rohli, R. V. & Li, C. in *Meteorology for Coastal Scientists* (eds Rohli, R. V. & Li, C.) 77–90 (Springer Int. Publ., 2021).
61. Collaud Coen, M. et al. Determination and climatology of the planetary boundary layer height above the Swiss plateau by in situ and remote sensing measurements as well as by the COSMO-2 model. *Atmos. Chem. Phys.* **14**, 13205–13221 (2014).
62. Tang, G. et al. Mixing layer height and its implications for air pollution over Beijing, China. *Atmos. Chem. Phys.* **16**, 2459–2475 (2016).
63. Wang, S. et al. Different chemical removal pathways of volatile organic compounds (VOCs): comparison of urban and regional sites. *Acta Sci. Circumst.* **40**, 2311–2322 (2020).

64. Dewald, P. et al. Fate of the nitrate radical at the summit of a semi-rural mountain site in Germany assessed with direct reactivity measurements. *Atmos. Chem. Phys.* **22**, 7051–7069 (2022).
65. Wang, H. et al. Increased night-time oxidation over China despite widespread decrease across the globe. *Nat. Geosci.* **16**, 217–223 (2023).
66. Yan, Y. et al. Vertically increased NO_3 radical in the nocturnal boundary layer. *Sci. Total Environ.* **763**, 142969 (2021).
67. Liebmann, J. et al. Direct measurement of NO_3 radical reactivity in a boreal forest. *Atmos. Chem. Phys.* **18**, 3799–3815 (2018).
68. Wang, H. et al. NO_3 and N_2O_5 chemistry at a suburban site during the EXPLORE-YRD campaign in 2018. *Atmos. Environ.* **224**, 117180 (2018).
69. Zhu, J. et al. Changes in NO_3 radical and its nocturnal chemistry in Shanghai from 2014 to 2021 revealed by long-term observation and a stacking model: impact of China's clean air action plan. *J. Geophys. Res. Atmos.* https://doi.org/10.1029/2022jd037438 (2022).
70. de Gouw, J. A. et al. Emission and chemistry of organic carbon in the gas and aerosol phase at a sub-urban site near Mexico City in March 2006 during the MILAGRO study. *Atmos. Chem. Phys.* **9**, 3425–3442 (2009).
71. Karl, T., Striednig, M., Graus, M., Hammerle, A. & Wohlfahrt, G. Urban flux measurements reveal a large pool of oxygenated volatile organic compound emissions. *Proc. Natl Acad. Sci. USA* **115**, 1186–1191 (2018).
72. Coggon, M. M. et al. Volatile chemical product emissions enhance ozone and modulate urban chemistry. *Proc. Natl Acad. Sci. USA* **118**, e2026653118 (2021).
73. Yang, Q. et al. Measurement report: Enhanced photochemical formation of formic and isocyanic acids in urban regions aloft – insights from tower-based online gradient measurements. *Atmos. Chem. Phys.* **24**, 6865–6882 (2024).
74. Aiken, A. C. et al. Mexico city aerosol analysis during MILAGRO using high resolution aerosol mass spectrometry at the urban supersite (T0) – part 2: analysis of the biomass burning contribution and the non-fossil carbon fraction. *Atmos. Chem. Phys.* **10**, 5315–5341 (2010).
75. Hodzic, A. et al. Modeling organic aerosols during MILAGRO: importance of biogenic secondary organic aerosols. *Atmos. Chem. Phys.* **9**, 6949–6981 (2009).
76. Park, J. H., Fares, S., Weber, R. & Goldstein, A. H. Biogenic volatile organic compound emissions during BEARPEX 2009 measured by eddy covariance and flux–gradient similarity methods. *Atmos. Chem. Phys.* **14**, 231–244 (2014).
77. Brown, S. S. et al. Cavity enhanced spectroscopy for measurement of nitrogen oxides in the Anthropocene: results from the Seoul tower during MAPS 2015. *Faraday Discuss.* **200**, 529–557 (2017).
78. Tang, G. et al. Modelling study of boundary-layer ozone over northern China - part I: ozone budget in summer. *Atmos. Res.* **187**, 128–137 (2017).
79. Takeuchi, M., Berkemeier, T., Eris, G. & Ng, N. L. Non-linear effects of secondary organic aerosol formation and properties in multi-precursor systems. *Nat. Commun.* **13**, 7883–7883 (2022).
80. Newland, M. J. et al. Low-NO atmospheric oxidation pathways in a polluted megacity. *Atmos. Chem. Phys.* **21**, 1613–1625 (2021).
81. Li, L. et al. Tower observed vertical distribution of $PM_{2.5}$, O_3 and NOx in the Pearl River Delta. *Atmos. Environ.* https://doi.org/10.1016/j.atmosenv.2019.117083 (2020).
82. Yan, F. et al. Stabilization for the secondary species contribution to $PM_{2.5}$ in the Pearl River Delta (PRD) over the past decade, China: a meta-analysis. *Atmos. Environ.* **242**, 117817 (2020).
83. Li, L. et al. Impact of the COVID-19 on the vertical distributions of major pollutants from a tower in the Pearl River Delta. *Atmos. Environ.* **276**, 119068 (2022).
84. He, X. et al. Volatile organic compounds in wintertime North China Plain: insights from measurements of proton transfer reaction time-of-flight mass spectrometer (PTR-ToF-MS). *J. Environ. Sci.* https://doi.org/10.1016/j.jes.2021.08.010 (2022).
85. Wu, C. et al. Measurement report: Important contributions of oxygenated compounds to emissions and chemistry of volatile organic compounds in urban air. *Atmos. Chem. Phys.* **20**, 14769–14785 (2020).
86. Wang, C. et al. Measurements of higher alkanes using NO^+ chemical ionization in PTR-ToF-MS: important contributions of higher alkanes to secondary organic aerosols in China. *Atmos. Chem. Phys.* **20**, 14123–14138 (2020).
87. Chen, Y. et al. Online measurements of cycloalkanes based on NO^+ chemical ionization in proton transfer reaction time-of-flight mass spectrometry (PTR-ToF-MS). *Atmos. Meas. Tech.* **15**, 6935–6947 (2022).
88. Wu, Y. et al. Quantitative impacts of vertical transport on the long-term trend of nocturnal ozone increase over the Pearl River Delta region during 2006–2019. *Atmos. Chem. Phys.* **23**, 453–469 (2023).
89. Alvarez, R., Weilenmann, M. & Favez, J.-Y. Evidence of increased mass fraction of NO_2 within real-world NOx emissions of modern light vehicles — derived from a reliable online measuring method. *Atmos. Environ.* **42**, 4699–4707 (2008).
90. Anttila, P., Tuovinen, J.-P. & Niemi, J. V. Primary NO_2 emissions and their role in the development of NO_2 concentrations in a traffic environment. *Atmos. Environ.* **45**, 986–992 (2011).
91. Xu, T. et al. Estimating hourly nitrogen oxide emissions over East Asia from Geostationary Satellite Measurements. *Environ. Sci. Technol. Lett.* **11**, 122–129 (2023).

Acknowledgements

This work was financially supported by the National Key R&D Plan of China (grant No. 2023YFC3710900, 2023YFC3706103, 2023YFC3706201, 2022YFC3700604) and the National Natural Science Foundation of China (grant No. 42121004, 42275103, 42230701, 42305095). This work was also supported by the Special Fund Project for Science and Technology Innovation Strategy of Guangdong Province (Grant No. 2019B121205004), Guangdong Basic and Applied Basic Research Foundation (Grant No. 2024A1515011570), Guangzhou Basic and Applied Basic Research Foundation (Grant No. 2024A04J3958). The authors would like to thank the personnel who participated in data collection, instrument maintenance, and logistic support during the field campaign.

Author contributions

B.Y. and X.B.L. conceived the research. X.S., X.B.L., X.J.H., Y.B.C., S.H.W., Y.B.H., Y.W.P., C.S.Z., A.M.L., H.L.Y., C.F.L., J.L., and M.S. contributed to the data collection. X.S., X.B.L., and B.Y. contributed to the data analysis. B.Y., X.B.L., and X.S. designed and performed the ozone source apportionment method. All the coauthors discussed the results and reviewed the paper.

Competing interests

The authors declare no competing interests.

Additional information

Supplementary information The online version contains supplementary material available at https://doi.org/10.1038/s41612-024-00818-8.

Correspondence and requests for materials should be addressed to Xiao-Bing Li or Bin Yuan.